Dynamics of Omnidirectional IPMC Sensor: Experimental Characterization and Physical Modeling

Hong Lei, Montassar Aidi Sharif, and Xiaobo Tan, *Senior Member, IEEE*

***Abstract*—Typical ionic polymer-metal composite (IPMC) sensors are in the shape of beams, and only respond to stimuli acting perpendicular to the beam plane. In this paper, we present a novel, omnidirectional, tubular IPMC sensor that responds to all stimuli perpendicular to the tube axis. With one common inner electrode and four outer electrodes, the tubular IPMC sensor provides four routes of common-ground current outputs. With a custom-made setup, the response of each sensor route is characterized under tip deflection in different orientations at frequencies 1–20 Hz, which verifies the sensor's omnidirectional sensing capability and shows little mechanoelectrical coupling between neighboring sensor routes. An analytical dynamic model, in the form of an infinite-dimensional transfer function, is developed for the sensor, which captures the internal ion-transport physics and the effect of contact resistance. Experimental results show that the proposed model is able to capture the tubular sensor dynamics. Finally, the original model is reduced to a finite-dimensional one, based on which an inversion algorithm is used to reconstruct the mechanical stimulus given the sensor output. The effectiveness of the reconstruction approach is demonstrated experimentally.**

***Index Terms*—Characterization, electroactive polymer, IPMC, modeling, omnidirectional sensing.**

I. Introduction

As one important class of electroactive polymers, ionic polymer-metal composites (IPMCs) have built-in sensing and actuation capabilities [1], [2]. Because of their inherent polarity, capability to work in water, high sensitivity, and direct mechanosensory property, IPMCs hold strong promise for versatile sensing applications [3], [4], including measurement of displacement [5], flow [6], shear loading [7], curvature [8], structural health monitoring [9], and energy harvesting [10]–[13]. They are also bio-compatible and amenable to fabrication [14]–[19]. An IPMC sensor is typically fabricated by chemically plating a layer of noble metal (e.g., platinum) as electrodes on both surfaces of a thin ion-exchange membrane (e.g., Nafion) [14], [20]. Inside the polymer, only cations can move freely in the membrane while anions are covalently fixed to polymer chains. An applied force or deformation on an IPMC beam would redistribute the cations and accompanying solvent molecules inside the polymer, leading to the generation of a detectable electrical signal (typically open-circuit voltage or short-circuit current) across the electrodes. Some of the recent studies on modeling of IPMC can be found in [9] and [21]–[27].

Reported IPMC sensors are typically in the shape of beams since they are often fabricated using thin Nafion films. Such IPMC sensors only respond to mechanical stimuli in the beam-bending direction (i.e., the direction perpendicular to the beam plane). Recently, several groups have demonstrated IPMC actuators of tubular [28] and cylindrical [29] shapes that can bend in all directions under an appropriate voltage stimulus, but the sensing property of these IPMCs has not been studied. Kim's group has examined a tube-shaped IPMC transducer [30] through finite element simulations, and experimentally investigated its use as multidirectional sensor devices. IPMC pipes and their buckling effect have also been reported [31]. Our group previously proposed an IPMC sensor with a shape of square column, fabricated based on Nafion cast [32]. However, the sensor showed strong mechanoelectrical coupling effect between different sensing routes, making it challenging to develop analytical models and reconstruct the stimuli.

In this paper, we first present a new fabrication process for an IPMC sensor capable of omnidirectional sensing. The sensor is a thin-wall tubular IPMC fabricated with Nafion tubing. It has one common inner electrode and four outer electrodes, which form four routes of common-ground sensor outputs. With a custom-designed experimental setup, we further characterize the sensor response (sensing current) to tip deflection in different directions. The setup provides dynamic tip bending with adjustable orientations and controlled bending amplitude and frequency (1 to 20 Hz). As the orientation angle varies, it is observed that antagonistic routes generally have similar periodic properties with opposite signal polarities, while neighboring routes show a shift of response by approximately 90°.

Based on the characterization results, we propose a physical dynamic model for the tubular IPMC sensor, by treating each infinitesimal slice (along the tube axis) of the tube as a beam-shaped IPMC sensor and performing integration around the tube. A governing partial differential equation (PDE) first introduced in [33] is used to describe the charge dynamics within IPMC, where the effect of contact resistance is captured. The model, which takes the form of an infinite-dimensional transfer

Manuscript received March 12, 2015; revised June 15, 2015; accepted August 3, 2015. Date of publication August 12, 2015; date of current version February 24, 2016. Recommended by Technical Editor F. Carpi. This work was supported in part by the National Science Foundation (DBI 0939454) and the Office of Naval Research (N000141210149, N000141512246).

The authors are with the Department of Electrical and Computer Engineering, Michigan State University, East Lansing, MI 48824 USA (e-mail: leihongbuaa@gmail.com; engmas83@yahoo.com; xbtan@egr.msu.edu).

Color versions of one or more of the figures in this paper are available online at http://ieeexplore.ieee.org.

Digital Object Identifier 10.1109/TMECH.2015.2468080

function, is further reduced to a finite-dimension model, based on which a scheme is developed for computing the tip deflection stimulus given the sensor outputs. Experiments have been conducted to validate the proposed model and the stimulus-reconstruction scheme.

A preliminary version of this study was presented at the 2014 SMASIS Conference [34]. The enhancements of this paper over [34] include: 1) improved modeling of the tubular IPMC sensor, which captures the effect of contact resistance and removes the restrictive assumption in [34] that antagonistic routes need to be perfectly symmetric with each other, and 2) model reduction and stimulus reconstruction along with the corresponding experimental results.

The remainder of the paper is organized as follows. The fabrication and packaging process for the proposed tubular IPMC sensor is presented in Section II. Sensor characterization results are discussed in Section III. The dynamic sensor model is presented in Section IV along with model reduction and experimental model validation results. Stimulus reconstruction and the related experimental results are discussed in Section V. Finally, concluding remarks and future work are provided in Section VI.

II. Sensor Fabrication and Packaging

A. Tubular IPMC Fabrication

The fabrication of the tubular IPMC uses Nafion tubing (TT-110, Perma Pure LLC) as the starting material, and the process flow otherwise follows the traditional IPMC fabrication approach [14]. First, the Nafion tubing is boiled in dilute hydrochloric acid (2 wt %) for an hour to release the internal stress and remove impurities. Then the tubing is boiled in the deionized (DI) water for another hour to further release the stress and remove the acid. After these pretreatments, the tubing is submerged in a platinum complex solution ($[Pt(NH_3)_4]Cl_2$) overnight so that the platinum ions would diffuse into the Nafion polymer and exchange with the hydrogen ions. Followed by the DI water rinse, the Nafion tubing is gently stirred in a water bath where the reducing agent of sodium borohydride solution (5 wt % $NaBH_4$ aq) is added for every half an hour with the amount of 2 ml, as the temperature of the water bath is raised from 40 °C to 60 °C gradually. After the reduction process, the platinum is deposited on the inner and outer surfaces as electrodes. To reduce the surface resistance, a second deposition of platinum is conducted by repeating those steps from the acid treatment to the reduction. The tubular IPMC sensor reported in this study has an inner diameter of 2.24 mm, outer diameter of 2.77 mm, wall thickness of 265 μm, and length of 30 mm.

B. Sensor Packaging

Before we use the fabricated tubular IPMC as a sensor, we first need to cut off the two tubing ends to avoid short circuit between the inner and outer electrodes. The outer electrode is then patterned into four subelectrodes equally, while the inner electrode is left untouched. In particular, a 3-D-printed device is used to facilitate the electrode patterning, as shown in Fig. 1. The tubular IPMC is first fit on the holding stick and covered

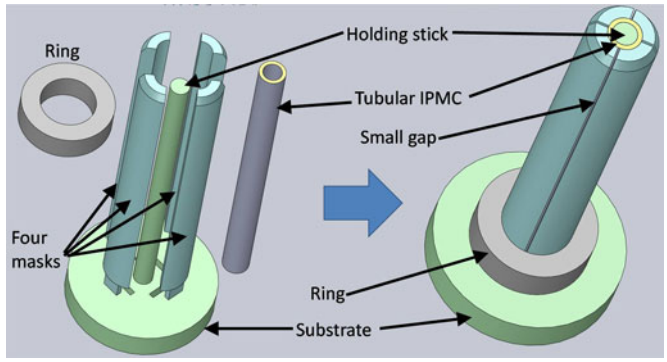

Fig. 1. 3-D-printed device for patterning the outer electrode.

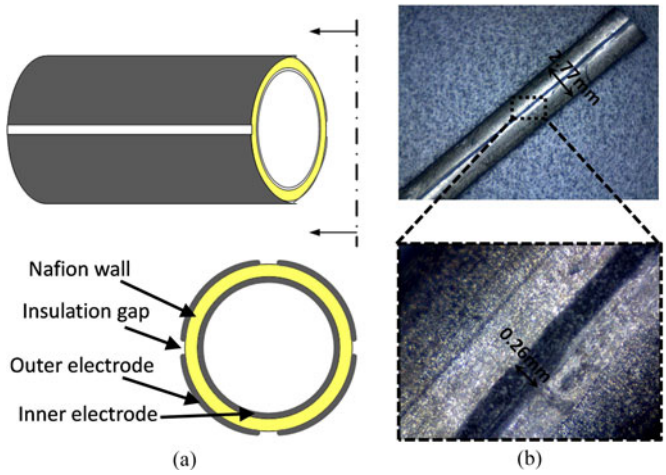

Fig. 2. Tubular IPMC with four equally divided outer electrodes: (a) Illustration (dimensions are not to scale); (b) real picture.

with four mask pieces. The diameter of the holding stick is the same as the inner diameter of the tubular IPMC, so that the fitting is tight. The four mask pieces are designed to form a tubular shape with small gaps (around 0.2 mm) between the neighboring pieces. Then a blade is used to manually scratch the surface of the outer electrode through the gaps, which is conducted carefully and gently to avoid cutting into the polymer. Fig. 2 shows the tubular IPMC sensor with four equally divided outer electrodes.

Compared with the common beam-shaped IPMC sensors, it is relatively difficult to connect conductive wires to the electrodes of the tubular IPMC. A custom-made apparatus is used to make electrical contacts for the sensor. A substrate is first 3-D-printed, with a base stem on the center to hold the tubular IPMC and with hollow arrows on the surface for the alignment purpose. Bare copper wires are then wrapped around the loading area of the stem to achieve perfect peripheral contact between the wires and the inner electrode. Note that the stem is only 3.5 mm long and used to hold the sensor base only, so the tubular IPMC can still bend freely. After the sensor is placed on the base stem and its insulation gaps are aligned with the hollow arrows, four base covers attached with wires are inserted into the substrate to connect the conductive wires to each outer subelectrode. At last, the base covers are fastened by a ring to enhance the contact.

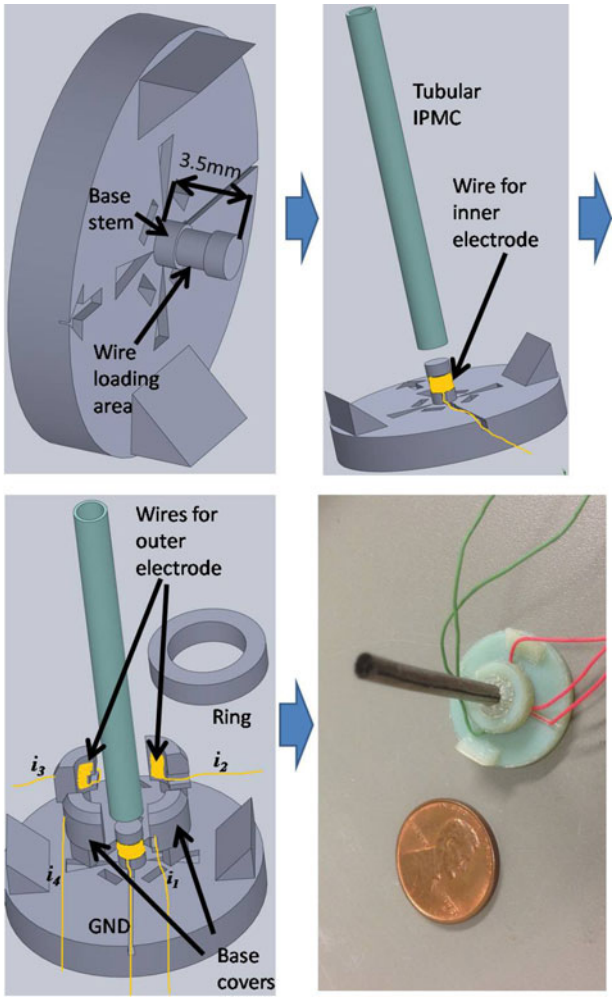

Fig. 3. Packaging and wiring scheme of a tube IPMC sensor.

The completed tubular IPMC sensor has five wires, as shown in Fig. 3. There are several ways to configure these wires as outputs. One configuration is to ignore the inner electrode and use each pair of wires (i_1 and i_3, or, i_2 and i_4) as one route. This configuration would suffer from severe electrical coupling between the two routes through inner electrode. Unless noted, for the rest of the paper, we adopt a four-route configuration, where the wire connected with the inner electrode is used as the common ground and the other four wires are used as separate sensor signals, as shown in Figs. 3 and 5. These four wires and their sensing currents, both denoted as i_1, i_2, i_3 and i_4, are defined as route 1, 2, 3, and 4.

III. Sensor Characterization

A. Experimental Setup

To evaluate its omnidirectional sensing behavior, we subject the tubular IPMC sensor to tip bending at different orientations. Fig. 4 shows the experimental setup, including a custom-designed angle plate, on which the tubular IPMC sensor package can be mounted with different orientations by aligning the

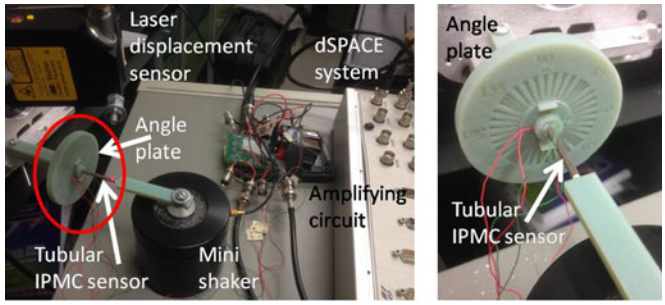

Fig. 4. Experimental setup for the characterization of the tubular IPMC sensor.

hollow arrow on the sensor substrate (see Fig. 3) with the angle scale (from 0° to 360°) on the angle plate. The angle plate together with the tubular IPMC sensor package is fixed on an aluminum frame, while the tip of the IPMC sensor is excited by a 3-D-printed stick, which is mounted on a minishaker (Type 4810, Brüel and Kjær). The shaker generates vibration stimuli with frequencies ranging from 1 to 20 Hz. The vibration orientation of the shaker is fixed (up and down), and its amplitude is controlled to be 2 mm. A laser displacement sensor (OADM 20I6441/S14F, Baumer Electric) is mounted above the tubular IPMC sensor to measure its tip displacement. The mounting frame for the laser sensor is isolated from the table where the minishaker is placed. A two-tier, four-channel amplification circuit [35] is used to measure the short-circuit currents in all four routes of the IPMC sensor. Control signal generation, sensing data acquisition, and processing are all performed through a dSPACE system.

Starting from 0° on the angle plate for the sensor orientation, frequency responses of all four routes under tip excitations are collected every 10°. Fast Fourier transform is used to extract the amplitudes of the four sensor outputs and the tip displacements at each frequency and each orientation, which are used to evaluate the sensor performances. Unless noted otherwise, all the data points in the rest of this paper are processed in this way and presented in the form of gain and phase shift, with the tip displacement as the input and the four routes of sensing currents as the outputs. For the convenience of discussion, we fix the local 2-D coordinate system $x - y$ in the cross-sectional plane of the tubular IPMC sensor, and the orientation of the tip excitation $u(t)$ in this coordinate system is denoted as γ, as illustrated in Fig. 5. Note that the wall of the IPMC sensor is divided into four portions denoted as A to D, corresponding to four routes 1 to 4.

B. Characterization Results and Discussion

1) Frequency Responses at a Fixed Orientation: Empirical frequency responses of all four routes of the tubular IPMC sensor are first examined for some fixed-orientation tip excitation. Fig. 6 shows the experimental results when the orientation angle γ is fixed at 45°. For the frequency response of each route, it can be seen that, with an increasing frequency (within the tested range) the magnitude increases while the phase shift (for the most part) drops. The latter trend represents similarity

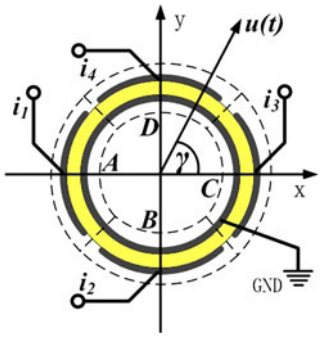

Fig. 5. Local 2-D coordinate system in the cross section of the tubular IPMC.

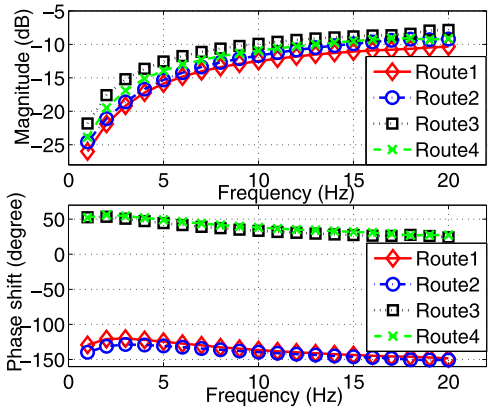

Fig. 6. Measured frequency responses at the stimulus orientation of 45°.

to that observed in beam-shaped IPMC sensors [9], [36]. Comparing different routes in Fig. 6, one can see that the sensing responses of all four routes have slightly different magnitudes at each frequency, which is not expected at the orientation angle of 45°. Due to the symmetric configuration shown in Fig. 5, the signal amplitudes of all four routes are expected to be equal when the orientation angle is 45°, 135°, 225° or 315°. The differences of sensitivity among the four routes are believed to be caused by the inhomogeneous material properties formed during the IPMC fabrication process, the imperfect patterning of the outer electrode, and the different contact resistances for the routes. The proposed model in Section IV will capture the effect of contact resistance.

The phase shifts for all the routes in Fig. 6 show excellent consistency and their relationships match expectations. For example, route 4 and route 3 always have phase shifts close to each other at every frequency, while route 4 and route 1 always have a phase difference close to 180°. This can be explained by the axial stress distribution as illustrated in Fig. 7 for $\gamma = 45°$. In particular, the axial stress distributions on segments A and D (likewise for segments B and C) are always skew-symmetric, and thus the sensing currents of routes 1 and 4 always have a phase difference of 180°. Similarly, at $\gamma = 45°$, routes 1 and 2 (and routes 3 and 4) always have the same polarities.

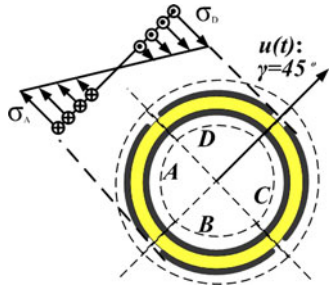

Fig. 7. Illustration of axial stress distribution for route 1 and 4 at the orientation stimulus of 45°.

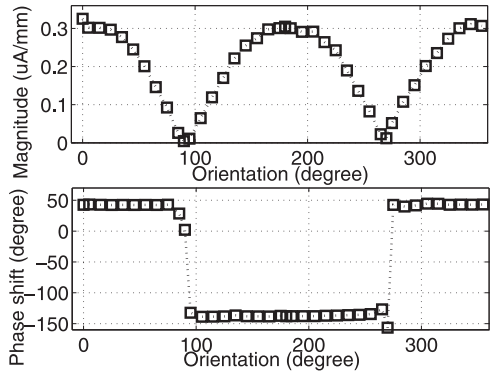

Fig. 8. Measured sensor response of route 3 at varying stimulus orientations at the frequency of 5 Hz.

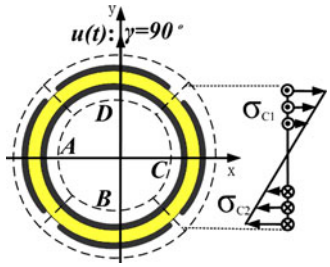

Fig. 9. Illustration of stress distribution for route 3 at the stimulus orientation of 90°.

2) Sensor Responses Under Omnidirectional Stimulus: The response of the tubular IPMC sensor is further characterized with the tip excitation applied at different orientations. Fig. 8 shows the response of route 3 at the fixed frequency of 5 Hz. Similar trends are observed at other frequencies. Note that the unit of the frequency response magnitude has been changed from decibel to the physical unit of $\mu\mathrm{A/mm}$ to present the experimental results more directly. First, one can see that there exists some periodic trend for the sensing response as the tip-excitation orientation γ varies. In particular, when γ is close to 90° and 270°, the signal magnitude drops to almost zero and the phase shift jumps with reversed polarity. This can be explained qualitatively by the induced normal stress distributed on the specific region of segment C (corresponding to route 3) in the tube cross section, as shown in Fig. 9. When the

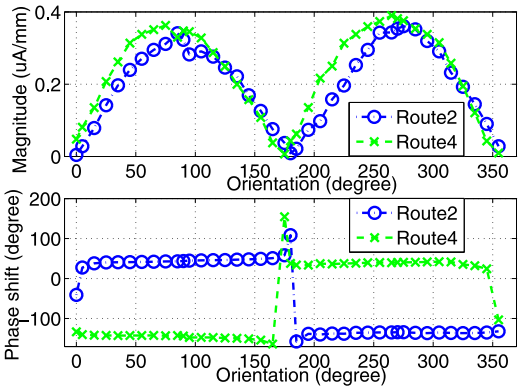

Fig. 10. Measured sensor responses of routes 2 and 4 at varying stimulus orientations at 10 Hz.

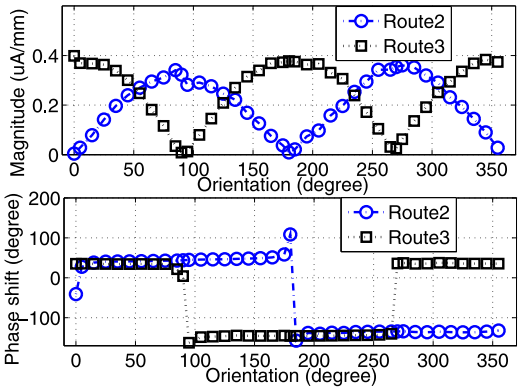

Fig. 11. Measured sensor responses of routes 2 and 3 at varying stimulus orientations at 10 Hz.

excitation is along the orientation of 90° or 270°, the upper and lower parts of C (with respect to the x-axis) have skew-symmetric induced stress distribution, canceling out each other's contributions to the sensing output. In addition, except around several jumping points, the phase shift maintains consistent, indicating that the varying orientations of the tip excitation only affect the signal polarity of each route while the phase shift is primarily determined by the charge dynamics inside the tubular IPMC.

Figs. 10 and 11 show the sensor responses at 10 Hz at varying orientations for antagonistic routes and neighboring routes, respectively. Note that similar responses have been observed at other frequencies. First, one can see that all the routes have similar trends as shown in Fig. 8, including the periodic feature of the magnitude response and the jumping points in the phase shift. In particular, for a pair of antagonistic routes, like 2 and 4 in Fig. 10, they generally have similar periodic properties except that their signal polarities are opposite. For a pair of neighboring routes, like 2 and 3 in Fig. 11, their sensing responses (both magnitude and phase shift) have a shift of about 90° with respect to the stimulus orientation angle. These characterization results suggest that the relationships between the sensing outputs of different routes are primarily determined by the mechanical coupling. In other words, the tubular IPMC

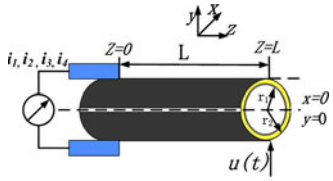

Fig. 12. Configuration of the tubular IPMC sensor subjected to the tip excitation $u(t)$.

sensor can be treated as a mechanical combination of four separate IPMC sensors through a tubular structure.

IV. Physical Modeling

A. Modeling Assumptions

Based on the experimental results and discussions in Section III, we propose a dynamic physical model for the tubular IPMC sensor under tip excitation. Consider Fig. 12, where the tubular IPMC with the length of L is clamped at the base and subjected to a tip displacement $u(t)$, producing four routes of sensing current $i_1(t)$ to $i_4(t)$. The xy plane is parallel to the cross section of the tube. The axis of the tube goes through the origin ($x = 0$ and $y = 0$) on each cross section. The outer radius and the inner radius are denoted by r_2 and r_1, respectively. The wall thickness is denoted by $2h = r_2 - r_1$. We assume that the tubular IPMC sensor is geometrically symmetric and the widths of the insulation gaps on the outer electrode are negligible. With two platinum deposition steps, the surface resistances of the inner and outer electrodes are very small and thus we assume the surface electrodes to be perfectly conductive. Note that the contact resistance between the surface electrode and the conductive wire for each route is not ignored, because the conductive wire is not soldered onto the surface electrode, which results in relatively large contact resistance. Considering that the wall thickness of the IPMC sensor is much smaller than the tube diameter, we further assume that the electric field E within the polymer of the tube wall is restricted to the normal directions of the tube surface, which is similar to the assumption made for traditional beam-shape IPMCs [33]. Since the sensor base is fixed and the sensor tip is subjected to prescribed deflection, we consider that the mechanical deformation of the tube is quasi-static under the relatively low-frequency (up to 20 Hz) tip stimuli. Finally, we assume that the tube excitation is sufficiently small, and therefore, the Brazier effect [37] of the tube bending is ignored.

B. Overview of the Modeling Approach

We consider an arbitrary excitation $u(t)$ with an orientation angle of γ, as shown in Fig. 13. $u(t)$ can be decomposed into two components of $u_x(t) = u(t)\cos\gamma$ and $u_y(t) = u(t)\sin\gamma$ in the x- and y-direction, respectively. We first model the sensor outputs induced by $u_y(t)$, as shown in Fig. 14. Now we consider an infinitesimal slice $p_{\mathrm{d}\alpha}$ on the tube wall with the length of L and the thickness of $2h$. The angle from $p_{\mathrm{d}\alpha}$ to $u_y(t)$ is denoted as α (radian), so the width of $p_{\mathrm{d}\alpha}$ is approximated as

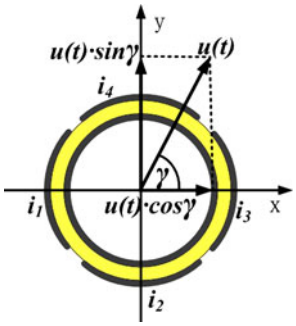

Fig. 13. Decomposition of the tip excitation.

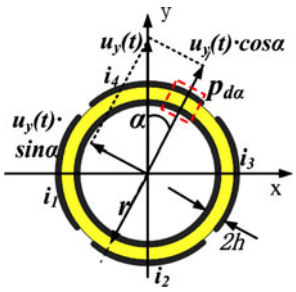

Fig. 14. Cross section of the tubular IPMC sensor subjected to the tip excitation.

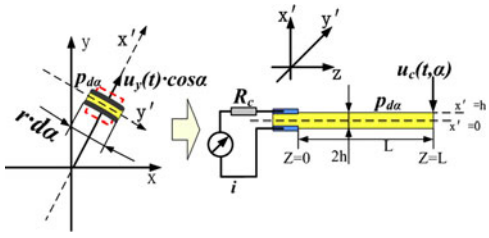

Fig. 15. One infinitesimal part $p_{\mathrm{d}\alpha}$ on the cross section.

$W = r \cdot \mathrm{d}\alpha$, where $r = (r_1 + r_2)/2$. The contact resistance for $p_{\mathrm{d}\alpha}$ is denoted as $R_c = R(j)\frac{0.5\pi}{\mathrm{d}\alpha}$, where $R(j), j = 1, 2, 3, 4$, is the measured contact resistance for route j that $p_{\mathrm{d}\alpha}$ belongs to. Then the displacement $u_y(t)$ can be decomposed into two components of $u_c(t, \alpha) = u_y(t)\cos\alpha$ and $u_s(t, \alpha) = u_y(t)\sin\alpha$, as shown in Fig. 14. Following the assumption that the electric field E inside the polymer is restricted to the radial direction, $p_{\mathrm{d}\alpha}$ only responds to $u_y(t)\cos\alpha$. Thus, $p_{\mathrm{d}\alpha}$ can be treated as a traditional beam-shaped IPMC with the width of $r \cdot \mathrm{d}\alpha$ and the thickness of $2h$, as shown in Fig. 15 where a new coordinate system $x' - y'$ for the cross section has been set up for the convenience of discussion. Following the similar derivation as in [36], the induced sensing current from $p_{\mathrm{d}\alpha}$ can be obtained by incorporating certain boundary conditions that are determined by the stress distribution and the contact resistance. At last, the total sensing current for each route induced by $u_y(t)$ can be obtained by integrating the sensing current of $p_{\mathrm{d}\alpha}$ around the tube for the given route. Similarly, we can model the sensor outputs induced by $u_x(t)$. Further details are provided in Section IV-C and D.

C. Modeling of the Sensing Output From Slice $p_{\mathrm{d}\alpha}$

As shown in Fig. 15, $p_{\mathrm{d}\alpha}$ can be viewed as a beam-shaped IPMC sensor. We can model the sensing response of $p_{\mathrm{d}\alpha}$ based on the governing PDE for charge density distribution ρ within IPMC [33], which is given by

$$\frac{\rho(x', z, t)}{\partial t} - d\frac{\partial^2 \rho(x', z, t)}{\partial (x')^2} + \frac{F^2 dC^-}{\kappa_e RT}(1 - C^- \triangle V)\rho(x', z, t) = 0 \tag{1}$$

where F is Faraday's constant, R is the gas constant, T is the absolute temperature, d is the ionic diffusivity, κ_e is the effective dielectric constant of the polymer, C^- is the anion concentration $(\mathrm{mol}/\mathrm{m}^3)$, and $\triangle V$ is the molar volume change which quantifies the cation hydrophilicity.

The exact solution to (1) can be obtained in the Laplace domain with appropriate boundary conditions, which are determined based on the assumption [36] that the charge density $\rho(x', z, s)$ is proportional to the mechanically induced stress $\sigma(x', z, s)$ at the boundary $x' = \pm h$. Note that even though $p_{\mathrm{d}\alpha}$ is treated as a beam structure here, the stress $\sigma(x', z, s)$ on $p_{\mathrm{d}\alpha}$ is still calculated based on the tubular structure, as shown in the complete derivation given in Appendix A. In particular, we can derive, for $-h \le x' \le h$

$$\rho(x', z, s) = a_1(z, s)e^{-\beta(s)x'} + a_2(z, s)e^{\beta(s)x'} \tag{2}$$

where $\beta(s) = \sqrt{\frac{s+K}{d}}$, $K \triangleq \frac{F^2 dC^-}{\kappa_e RT}(1 - C^- \triangle V)$, and $a_1(z, s)$ and $a_2(z, s)$ are as given in Appendix A.

Let D, E, and ϕ denote the electrical displacement, electric field, and electric potential, respectively. Then the following equations hold:

$$D(x', z, s) = \kappa_e E(x', z, s) \tag{3}$$

$$E(x', z, s) = -\frac{\partial \phi(x', z, s)}{\partial x'} \tag{4}$$

$$\kappa_e \frac{\partial E(x', z, s)}{\partial x'} = \rho(x', z, s). \tag{5}$$

With (2) and (5), we can solve for $E(x', z, s)$ for this infinitesimal part $p_{\mathrm{d}\alpha}$ using appropriate boundary conditions at $x' = \pm h$. With the assumption that the inner and outer electrodes are perfectly conductive, the electric potential is uniform across both surfaces $x' = \pm h$. Since the inner electrode is used as the common ground, the potential $\phi(-h, z, s)$ is set to be zero. Due to the existence of the contact resistance, the sensing currents of the tubular IPMC sensor are not treated as short-circuit currents; therefore, at $x' = h$ the potential $\phi(h, z, s) = R_c i(s)$ is not equal to zero but dependent on the contact resistance, as illustrated in Fig. 15. The sensing current is the time derivative of the induced charge $Q(t)$, which implies $i(s) = sQ(s)$, and the total induced sensing charge can be obtained by integrating the electrical displacement D on the boundary $x' = h$. Therefore, we have the following boundary conditions to solve for

$E(x', z, s)$ (see Appendix B for details):

$$\phi(-h, z, s) = 0 \tag{6}$$

$$\phi(h, z, s) = R_c s Q(s) = R_c s \int_0^L \int_0^W \kappa_e E(h, z, s) \mathrm{d}y' \mathrm{d}z. \tag{7}$$

With knowing $E(x', z, s)$, one can further derive the charge $Q(s)$ and the sensing current $i(s)$ induced on $p_{\mathrm{d}\alpha}$ based on the discussion above. To make the following discussion more clear, we use new notation, $\mathrm{d}Q(s, \alpha)$ and $\mathrm{d}i(s, \alpha)$, to replace the notation $Q(s)$ and $i(s)$, respectively. The sensing current on $p_{\mathrm{d}\alpha}$ is linear with respect to the external stimulus $u_c(s, \alpha)$

$$\begin{aligned}\mathrm{d}i(s, \alpha) = \frac{u_c(s, \alpha) 3YWhs}{\alpha_o L \beta^2(s)(R_c \kappa_e W L s + 2h)} (\beta(s)(e^{\beta(s)h}\beta_2(s) \\ - e^{-\beta(s)h}\beta_1(s) + (e^{-\beta(s)h} - e^{\beta(s)h}) \\ (\beta_2(s) - \beta_1(s))))\end{aligned} \tag{8}$$

where α_o is the charge-stress coupling constant, and

$$\beta_1(s) = \frac{r_2 - r_1 e^{2\beta(s)h}}{e^{-\beta(s)h} - e^{3\beta(s)h}} \tag{9}$$

$$\beta_2(s) = \frac{r_1 - r_2 e^{2\beta(s)h}}{e^{-\beta(s)h} - e^{3\beta(s)h}}. \tag{10}$$

D. Modeling of the Sensing Output From Each Route

Note that $p_{\mathrm{d}\alpha}$ is an infinitesimal part at angle α. The total induced sensing current for one route can be obtained by integrating $\mathrm{d}i(s, \alpha)$ over α. Take route 1 for example. We denote R_1 as the measured contact resistance of route 1, and plug $R_c = R_1 \frac{0.5\pi}{\mathrm{d}\alpha}$, $W = r \cdot \mathrm{d}\alpha$, and $u_c(s, \alpha) = u_y(s) \cos\alpha$ into (8)

$$\mathrm{d}i(s, \alpha) = \frac{i_0(s)}{\frac{\pi}{2} R_1 \kappa_e r L s + 2h} u(s) \cos\alpha \mathrm{d}\alpha \tag{11}$$

$$\begin{aligned}\text{with } i_0(s) = \frac{3Yrhs}{\alpha_o L \beta^2(s)} (\beta(s)(e^{\beta(s)h}\beta_2(s) - e^{-\beta(s)h}\beta_1(s)) \\ + (e^{-\beta(s)h} - e^{\beta(s)h})(\beta_2(s) - \beta_1(s))).\end{aligned} \tag{12}$$

We can then integrate (11) from $\alpha = \frac{5\pi}{4}$ to $\alpha = \frac{7\pi}{4}$ for route 1, and obtain the total sensing current induced by the $y-$component of $u(s)$ (recall Fig. 14) as

$$i_{1y}(s) = \int_{\frac{5\pi}{4}}^{\frac{7\pi}{4}} \frac{i_0(s)}{\frac{\pi}{2} R_1 \kappa_e r L s + 2h} u(s) \cos\alpha \mathrm{d}\alpha = 0. \tag{13}$$

Similarly, the total sensing currents induced by $u_y(s)$ for other routes are given by

$$i_{2y}(s) = \frac{-\sqrt{2} i_0(s)}{\frac{\pi}{2} R_2 \kappa_e r L s + 2h} u(s) \tag{14}$$

$$i_{3y}(s) = 0 \tag{15}$$

$$i_{4y}(s) = \frac{\sqrt{2} i_0(s)}{\frac{\pi}{2} R_4 \kappa_e r L s + 2h} u(s). \tag{16}$$

TABLE I
PHYSICAL CONSTANTS AND DIRECTLY MEASURED PARAMETERS

F	R	T	L	r_1	r_2
(C mol^{-1})	(J mol^{-1}K^{-1})	(K)	(mm)	(mm)	(mm)
96487	8.3143	290	30	1.10	1.38
$h(\mu\mathrm{m})$	r(mm)	$R_1(\Omega)$	$R_2(\Omega)$	$R_3(\Omega)$	$R_4(\Omega)$
140	1.24	5.0	3.4	6.1	4.8

Now considering the sensing outputs due to the $x-$component of the input, $u_x(t) = u(t)\cos\gamma$, we have

$$i_{1x}(s) = \frac{-\sqrt{2} i_0(s)}{\frac{\pi}{2} R_1 \kappa_e r L s + 2h} u(s) \tag{17}$$

$$i_{3x}(s) = \frac{\sqrt{2} i_0(s)}{\frac{\pi}{2} R_3 \kappa_e r L s + 2h} u(s) \tag{18}$$

$$i_{2x}(s) = i_{4x}(s) = 0. \tag{19}$$

Based on the results from (13) to (17), we can see that routes 1 and 3 only respond to the $x-$component of the tip stimulus, $u(t)\cos\gamma$, and routes 2 and 4 only respond to the $y-$ component of the stimulus, $u(t)\sin\gamma$. Hence, the complete dynamic model for the tubular IPMC sensor subjected to tip excitation $u(t)$ with the angle of γ is

$$H_1(s) = \frac{i_1(s)}{u(s)} = -C_1 \frac{H_0(s)}{\frac{\pi}{2} R_1 \kappa_e r L s + 2h} \cos\gamma \tag{20}$$

$$H_2(s) = \frac{i_2(s)}{u(s)} = -C_2 \frac{H_0(s)}{\frac{\pi}{2} R_2 \kappa_e r L s + 2h} \sin\gamma \tag{21}$$

$$H_3(s) = \frac{i_3(s)}{u(s)} = C_3 \frac{H_0(s)}{\frac{\pi}{2} R_3 \kappa_e r L s + 2h} \cos\gamma \tag{22}$$

$$H_4(s) = \frac{i_4(s)}{u(s)} = C_4 \frac{H_0(s)}{\frac{\pi}{2} R_4 \kappa_e r L s + 2h} \sin\gamma \tag{23}$$

$$\begin{aligned}\text{with } H_0(s) = \frac{3\sqrt{2} Yrhs}{\alpha_o L \beta^2(s)} (\beta(s)(e^{\beta(s)h}\beta_2(s) - e^{-\beta(s)h}\beta_1(s)) \\ + (e^{-\beta(s)h} - e^{\beta(s)h})(\beta_2(s) - \beta_1(s)))\end{aligned} \tag{24}$$

where additional constants C_1 to C_4 have been introduced to accommodate the sensitivity differences among different routes, as evidenced in Fig. 6 and discussed in Section III-B. Note that due to the assumption of quasi-static mechanical deformation, the complete dynamic model above only includes the dynamics for the electrical subsystem.

E. Model Reduction

The sensing model shown in (20) to (23) is infinite-dimensional since it involves irrational functions such as $e^{(\cdot)}$ and $\sqrt{\cdot}$. For practical implementation of stimulus reconstruction or feedback control design, it is of interest to reduce the model to a finite order. First, we take $1 - C^- \Delta V \approx 1$ since $|C^- \Delta V| \ll 1$[33]. Based on the measured and identified physical parameters (see Tables I and II in Section IV-F), for $s = j\omega$, one has $|\beta(s)h| = \left|h\sqrt{\frac{s+K}{d}}\right| > 100$ and $e^{-\beta(s)h} - e^{3\beta(s)h} \approx$

TABLE II
IDENTIFIED PARAMETERS BY CURVE-FITTING

C_1Y/α_o (Pa C J^{-1})	C_2Y/α_o (Pa C J^{-1})	C_3Y/α_o (Pa C J^{-1})	C_4Y/α_o (Pa C J^{-1})
1.30×10^5	2.05×10^5	2.41×10^5	2.39×10^5
d (m^2 s^{-1})	C^-(mol m^{-3})	κ_e(F m^{-1})	
3.308×10^{-12}	1086	3.1×10^{-3}	

$-e^{3\beta(s)h}$, when the angular frequency ω is relatively low. We can then simplify $\beta_1(s)$ as

$$\beta_1(s) \approx \frac{r_2 - r_1 e^{2\beta(s)h}}{-e^{3\beta(s)h}} \approx \frac{r_1}{e^{\beta(s)h}}. \tag{25}$$

Similarly, $\beta_2(s)$ can be simplified as $\frac{r_2}{e^{\beta(s)h}}$. Then we have

$$(e^{-\beta(s)h} - e^{\beta(s)h})(\beta_2(s) - \beta_1(s)) = \frac{2h}{e^{2\beta(s)h}} - 2h$$

$$\beta(s)(e^{\beta(s)h}\beta_2(s) - e^{-\beta(s)h}\beta_1(s)) = \beta(s)r_2 - \frac{\beta(s)r_1}{e^{2\beta(s)h}}$$

$$(e^{-\beta(s)h} - e^{\beta(s)h})(\beta_2(s) - \beta_1(s))$$
$$+ \beta(s)(e^{\beta(s)h}\beta_2(s) - e^{-\beta(s)h}\beta_1(s))$$
$$= \beta(s)r_2 - 2h + \frac{1}{e^{2\beta(s)h}}(2h - \beta(s)r_1)$$

where $\frac{1}{e^{2\beta(s)h}}(2h - \beta(s)r_1) \approx 0$, which yields

$$H_0(s) = \frac{3\sqrt{2}Yrhs(\beta(s)r_2 - 2h)}{\alpha_o L\beta^2(s)}.$$

Now, for example, the transfer function $H_1(s)$ of route 1 becomes

$$\hat{H}_1(s) = -C_1 \frac{H_0(s)}{\frac{\pi}{2}R_1\kappa_e rLs + 2h}\cos\gamma$$
$$= \frac{-3\sqrt{2}C_1Yrh\cos\gamma(\beta(s)r_2 - 2h)s}{\alpha_o L\beta^2(s)(\frac{\pi}{2}R_1\kappa_e rLs + 2h)}. \tag{26}$$

Plugging $\beta(s) = \sqrt{\frac{s+K}{d}}$ into (26), we have

$$\hat{H}_1(s) = \frac{6\sqrt{2d}C_1Yrh\cos\gamma s(\sqrt{s+K}r_2 - 2h\sqrt{d})}{\alpha_o L(\pi R_1\kappa_e rLs + 4h)(s+K)}. \tag{27}$$

To further reduce (27) to a finite order, we approximate $\sqrt{s+K}$ with a rational function of s based on Padé approximation [38]. It is found that the Padé approximation of the order (3/2) can provide adequate approximation with minimal complexity for $\sqrt{s+K}$ around some point s_0, where $s_0 = |j\omega_0|$ and ω_0 is close to the midpoint of the angular frequency range one is interested in. In this paper, we take $s_0 = 60$, because the frequency range considered in our experiments is from 1 to 20 Hz. The resulting finite-dimensional approximation to $H_1(s)$ is

$$\hat{H}_1(s) = \frac{6\sqrt{2d}C_1Yrh\cos\gamma s}{\alpha_o L}\frac{p_3s^3 + p_2s^2 + p_1s + p_0}{q_4s^4 + q_3s^3 + q_2s^2 + q_1s + q_0} \tag{28}$$

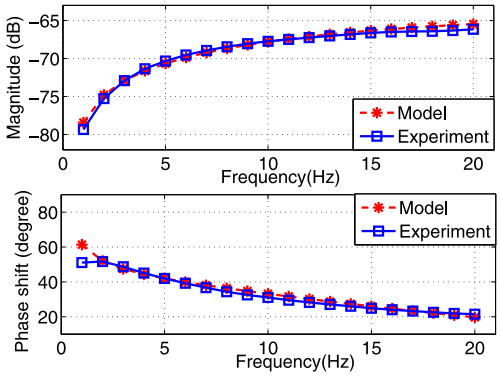

Fig. 16. Identification of some model parameters via curve-fitting for route 3 at 180° of stimulus orientation (input: tip excitation; output: IPMC sensing current).

where coefficients of $p_0, \ldots, p_3$ are dependent on [K, s_0, r_2, d, h], and coefficients of $q_0, \ldots, q_4$ are dependent on [K, s_0, h, R_1, κ_e, r, L].

With the same strategy, analogous results can be obtained for the other three routes. Note that the reduced model (28) is still a physics-based model since it is expressed in terms of fundamental physical parameters. The reduced model will be used for parameter identification, model validation, and stimulus reconstruction given the sensor output.

F. Model Validation

1) Parameter Identification: To validate the proposed model, physical parameters in the model need to be identified first. Table I lists the physical constants and the parameters obtained through direct measurement. For the measurement of contact resistances, a multimeter was used with one probe touching the outer electrode close to the base cover of one route (see Fig. 3) and the other probe connected to the end of the corresponding wire. The parameters that remain to be determined include the Young's modulus Y, compensation coefficients C_1 to C_4, diffusion coefficient d, anion concentration C^-, dielectric constant κ_e, and charge-stress coupling constant α_o, all of which are tuned by curve-fitting the empirical frequency responses of each route using the Matlab function $fminsearch$.

All the identified parameters are listed in Table II. For route 1, the frequency response at the orientation of 0° (or γ =180°) was used to identify its parameters, since at this orientation route 1 has largest sensing output. Similarly, the frequency responses at 90°, 180° and 270° were used for route 2, 3 and 4, respectively. Note that the Young's modulus Y, compensation coefficients C_1 to C_4, and charge-stress coupling constant α_o contribute the same scaling effect to the sensing model; see (28). Therefore, they cannot be identified separately and thus are treated as a whole in this study. Their different values in Table II (C_1Y/α_o to C_4Y/α_o) are believed to be caused by the inhomogeneous material properties formed during the IPMC fabrication process as well as the imperfect patterning of the outer electrode. Fig. 16 shows the result of curve-fitting for route 3, where the model predictions fit the experimental data well over the considered frequency range for both the magnitude and phase responses.

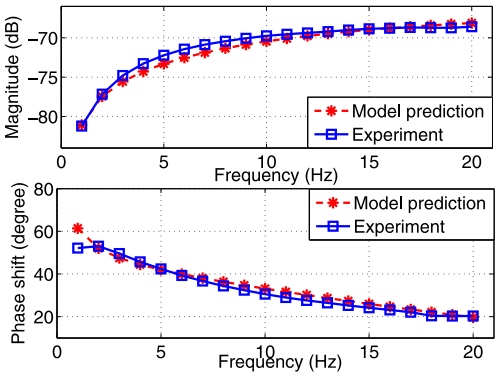

Fig. 17. Comparison of the measured frequency responses with model predictions for route 3 at 45° of orientation (input: tip excitation; output: IPMC sensing current).

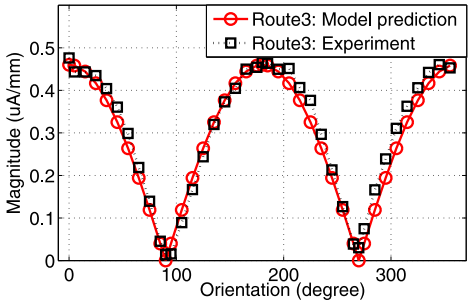

Fig. 18. Comparison of the measured frequency responses at 15 Hz with model predictions for route 3 at varying orientations (input: tip excitation; output: IPMC sensing current).

Given the Young's modulus, mass per unit length, and dimensions of the tube, the natural frequencies for a cantilevered tube can be calculated by the formula [39] $f_n = \frac{\lambda}{2\pi}\sqrt{\frac{YI}{mL^4}}$, where λ =3.52 is the frequency factor for the first mode, $I = \pi(r_2^4 - r_1^4)/4$ is the area moment of inertia, and $m = 4.3$ g/m is the measured mass per unit length. By plugging in the dimensions given in Table I and Young's modulus in Table II, we estimate the natural frequency of 54 Hz for the first-mode vibration of the tubular IPMC sample. Note that the value of Y is estimated by assuming all compensation coefficients to be 1, then averaging the identified C_1Y/α_o to C_4Y/α_o, and plugging in the nominal α_o from the literature [9], [36]. The estimated first-mode natural frequency indicates that the quasi-static assumption of the mechanical deformation introduced in Section IV-A is acceptable under the relatively low-frequency (up to 20 Hz) tip stimuli.

2) Model Validation: With the identified parameters, we first validate the proposed model in terms of the frequency responses. Fig. 17 shows the model prediction and the experimental data at the orientation of 45° for route 3. Note that the data at 45° were not used for parameter identification of route 3. As we can see in the figure, overall the model predictions have good agreement with the experimental data for both the magnitude and phase responses over the full frequency range, providing support for the physical nature of the proposed model. Fig. 18 shows the model-predicted and measured magnitudes of the frequency response at 15 Hz for route 3 at varying orientations. Again, one can see that good agreement is achieved, indicating the feasibility of the proposed modeling approach on omnidirectional sensing.

V. Stimulus Reconstruction

A. Inversion Algorithm

One novel feature of the proposed tubular IPMC sensor is its omnidirectional sensing capability, which can be potentially used for 2-D flow and displacement sensing. In such applications, one need to infer the 2-D mechanical stimulus given the sensing outputs of the IPMC sensor. In particular, it is of interest to reconstruct the original tip excitation signal $u(t)$ and the orientation angle γ based on the four routes of sensing outputs $i_1(t)$ to $i_4(t)$. Generally, for a single-input-single-output system, the reconstruction can be conducted by inverting the forward sensing model

$$u(s) = H_{inv}(s)i(s)$$

where $H_{inv}(s)$ denotes the inverse dynamics

$$H_{inv}(s) = \frac{1}{\hat{H}(s)}.$$

However, the tubular IPMC sensor has multiple inputs and outputs. As discussed in Section IV, we find that routes 1 and 3 only respond to the $x-$ component u_x of the stimulus $u(t)$, and routes 2 and 4 only respond to the $y-$ component u_y of $u(t)$. Therefore, we can reconstruct u_x and u_y separately. In the following, we will illustrate how to use route 1 to reconstruct u_x. The inverse dynamics for route 1 is

$$\begin{aligned} H_{inv1}(s) &= \frac{u_x(s)}{i_1(s)} = \cos\gamma \frac{1}{\hat{H}_1(s)} \\ &= \frac{\alpha_o L}{6\sqrt{2d}C_1 Yrhs} \frac{q_4 s^4 + q_3 s^3 + q_2 s^2 + q_1 s + q_0}{p_3 s^3 + p_2 s^2 + p_1 s + p_0}. \end{aligned} \tag{29}$$

The identified model for (28) has no zeros on the right half plane, so the inverse model (29) can be directly implemented except for the integrator (pole at the origin). In implementation, we approximate the pole with a pole at $-\epsilon > 0$. In particular, ϵ is chosen to be -0.1. This is reasonable since $s + 0.1 \approx s$ within the considered frequency range 1–20 Hz. We note that in the event that $\hat{H}_1$ has zeros on the right half plane, stable but noncausal inversion algorithms can be used [9], [35].

Similarly, the above algorithm is applied to the other routes. Since both routes 1 and 3 can be used to reconstruct u_x, we take the average of the reconstructed values from the two routes as the final prediction for u_x. An analogous approach is taken to reconstruct u_y based on the outputs from routes 2 and 4.

B. Experimental Results

Fig. 19(a) and (b) shows the experimental setup for the reconstruction of mechanical stimulus. A 3-D-printed square target is mounted to the tip of the tubular IPMC sensor, so that the

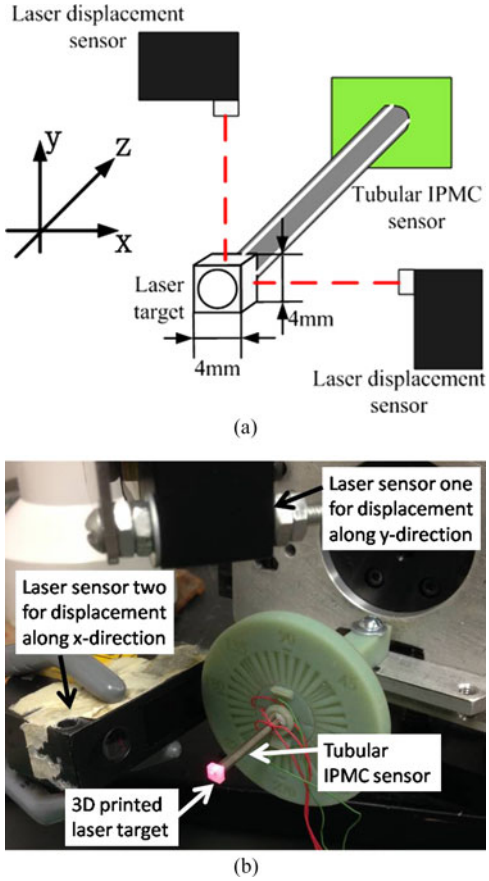

Fig. 19. Experimental setup from stimulus reconstruction: (a) schematic; (b) actual.

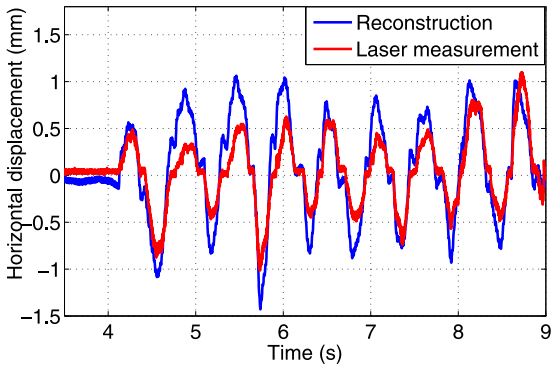

Fig. 20. Comparison of the horizontal displacement (x-axis) between the reconstruction and the direct measurement.

tip displacements in the x- and y-directions can be easily captured by two laser displacement sensors (OADM 20I6441/S14F; Baumer Electric). The laser target is hollow inside, so its gravity effect is minimized. In the experiments, we manually perturb the tip of the tubular IPMC with imposed displacements along arbitrary directions within the xy plane. The signals from two laser sensors are collected as the true excitation inputs u_x and u_y, while the signals from the four routes of the tubular IPMC sensor are used to reconstruct u_x and u_y. Figs. 20 and 21 show

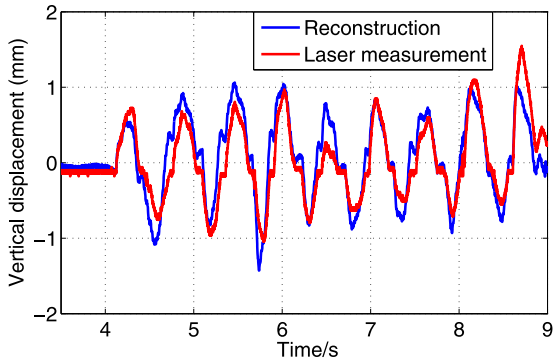

Fig. 21. Comparison of the vertical displacement (y-axis) between the reconstruction and the direct measurement.

the reconstructed tip excitation signals along x-axis and y-axis, respectively, with comparison with the direct measurements. It can be seen that there is a reasonable agreement between the reconstructed and measured deflections for each direction. The observed discrepancies can potentially be attributed to several factors, including unmodeled high-frequency dynamics excited by the irregular manual perturbation, and the impact of ambient temperature and humidity conditions, which could be mitigated by exploring several approaches in the relevant literature [35], [40], [41].

VI. Conclusion

In this paper, we have presented a novel IPMC sensor in the form of a thin-wall tubing. This tubular IPMC sensor responds to mechanical stimulus from any direction within the cross-sectional plane. We have characterized the sensor response in air. Based on the characterization results, we have considered the tubular IPMC sensor as a mechanical combination of four quarter-tube IPMC sensors, and developed a physical, dynamic model that incorporates the effect of contact resistance. We have further obtained a reduced model, which has been exploited for stimulus reconstruction. Experiments have been conducted to validate the proposed model and the reconstruction scheme, indicating that the proposed model well captures the sensor responses and the tubular IPMC sensor can be potentially used for 2-D flow and displacement sensing.

Future work will involve exploring encapsulation techniques [41] for the tubular IPMC sensor so that it can operate consistently under different media including water and other types of fluids. Its application to flow sensing will be subsequently pursued.

Appendix A
Derivation of the Charge Density ρ

Performing a Laplace transform for the time variable of $\rho(x', z, t)$, we can convert (1) into the Laplace domain

$$\frac{\partial^2 \rho(x', z, s)}{\partial (x')^2} - \beta(s)^2 \rho(x', z, s) = 0 \tag{30}$$

where $\beta(s) = \sqrt{\frac{s+K}{d}}$ and $K \triangleq \frac{F^2 dC^-}{\kappa_e RT}(1 - C^- \triangle V)$. The general solution of (30) takes the form

$$\rho(x', z, s) = a_1(z, s)e^{-\beta(s)x'} + a_2(z, s)e^{\beta(s)x'} \tag{31}$$

where $a_1(z, s)$ and $a_2(z, s)$, some appropriate functions depending on the boundary conditions, are determined based on the assumption that $\rho(x', z, s)$ is proportional to the mechanically induced stress $\sigma(x', z, s)$ at the boundary $x' = \pm h$

$$\sigma(\pm h, z, s) = \alpha_o \rho(\pm h, z, s) \tag{32}$$

where α_o is the charge-stress coupling constant.

The stress σ can be further related to the external stimulus. Consider the stress distribution on $p_{\mathrm{d}\alpha}$ when the tubing is excited by $u_c(t, \alpha)$ at the tip. In the time domain

$$\sigma(x', z, t) = \frac{M(z, t)(x' + r)}{I} \tag{33}$$

where $M(z, t)$ denotes the bending moment at z and I is the moment of inertia of the tubing. $M(z, t)$ can be related to the external force $F(t)$ at the tip by

$$M(z, t) = F(t)(L - z). \tag{34}$$

Given the assumption that the tip-excitation is quasi-static within the relatively low frequency range, the out-of-plane deflection $u_c(t, \alpha)$ at the tip can be related to the force $F(t)$ by [39]

$$u_c(t, \alpha) = \frac{L^3 F(t)}{3YI} \tag{35}$$

where Y is the Young's modulus of the tubing. Combining (33) to (35) and considering the stress at the boundary, we have

$$\begin{aligned} \sigma(h, z, t) &= \frac{3Y r_1 (L - z) u_c(t, \alpha)}{L^3} \\ \sigma(-h, z, t) &= \frac{3Y r_2 (L - z) u_c(t, \alpha)}{L^3}. \end{aligned} \tag{36}$$

Now back to Fig. 15, by transforming (36) into the Laplace domain and combining it with (32), we obtain

$$\begin{aligned} \rho(-h, z, s) &= \frac{3Y r_1 (L - z) u_c(s, \alpha)}{\alpha_o L^3} \\ \rho(h, z, s) &= \frac{3Y r_2 (L - z) u_c(s, \alpha)}{\alpha_o L^3} \end{aligned} \tag{37}$$

which, together with (31), yields

$$a_1(z, s) = \frac{3Y(L - z)u_c(s, \alpha)\beta_1(s)}{\alpha_o L^3} \tag{38}$$

$$a_2(z, s) = \frac{3Y(L - z)u_c(s, \alpha)\beta_2(s)}{\alpha_o L^3} \tag{39}$$

where

$$\beta_1(s) = \frac{r_2 - r_1 e^{2\beta(s)h}}{e^{-\beta(s)h} - e^{3\beta(s)h}} \tag{40}$$

$$\beta_2(s) = \frac{r_1 - r_2 e^{2\beta(s)h}}{e^{-\beta(s)h} - e^{3\beta(s)h}}. \tag{41}$$

Appendix B
Derivation of the Electrical Field E

Using (31) and the field equations (5) and (4), one can derive the expressions for the electrical field E and then for the electrical potential ϕ in the Laplace domain

$$E(x', z, s) = \frac{a_2(z, s)e^{\beta(s)x'} - a_1(z, s)e^{-\beta(s)x'}}{\kappa_e \beta(s)} + b_1(z, s) \tag{42}$$

$$\begin{aligned} \phi(x', z, s) = &\frac{-a_1(z, s)e^{-\beta(s)x'} - a_2(z, s)e^{\beta(s)x'}}{\kappa_e \beta^2(s)} - b_1(z, s)x' \\ &+ b_2(z, s) \end{aligned} \tag{43}$$

where $b_1(z, s)$ and $b_2(z, s)$ are appropriate functions to be determined based on the boundary conditions on ϕ. Plugging (42) into (7) and then combining (6) and (7) with (43), one can solve for $b_1(z, s)$

$$\begin{aligned} b_1(z, s) = &\\ &\frac{3Y u_c(s, \alpha)(L - z)(e^{-\beta(s)h} - e^{\beta(s)h})(\beta_2(s) - \beta_1(s))}{2\alpha_o h L^3 \kappa_e \beta^2(s)} \\ &+ \frac{3sY u_c(s, \alpha) R_c W}{4\alpha_o h L \beta^2(s)(sR_c\kappa_e WL + 2h)}(2h\beta(s)\beta_1(s)e^{-\beta(s)h} \\ &- 2h\beta(s)\beta_2(s)e^{\beta(s)h} + (e^{\beta(s)h} - e^{-\beta(s)h})(\beta_2(s) - \beta_1(s))). \end{aligned} \tag{44}$$

Combining (44), (42) and (3), one can obtain the electrical field E and the electrical displacement D.

References

[1] Y. Bar-Cohen, *Electroactive Polymer (EAP) Actuators as Artificial Muscles: Reality, Potential and Challenges*. Bellingham, WA, USA: SPIE Press, 2004.

[2] M. Shahinpoor and K. Kim, "Ionic polymer-metal composites: I. Fundamentals," *Smart Mater. Struct.*, vol. 10, pp. 819–833, 2001.

[3] M. Shahinpoor, Y. Bar-Cohen, J. Simpson, and J. Smith, "Ionic polymer-metal composites (IPMCs) as biomimetic sensors, actuators and artificial muscles - A review," *Smart Mater. Struct.*, vol. 7, no. 6, pp. R15–R30, 1998.

[4] M. Shahinpoor and M. Mojarrad, "Ionic polymer sensors and actuators," U.S. Patent 6 475 639, Nov. 5, 2002.

[5] R. Dong and Y. Tan, "A model based predictive compensation for ionic polymer metal composite sensors for displacement measurement," *Sensors Actuators A: Phys.*, vol. 224, no. 1, pp. 43–49, 2015.

[6] L. DeVries, F. D. Lagor, H. Lei, X. Tan, and D. A. Paley, "Distributed flow estimation and closed-loop control of an underwater vehicle with a multi-modal artificial lateral line," *Bioinspiration Biomimetics*, vol. 10, no. 2, pp. 025002-1–025002-10, 2015.

[7] U. Zangrilli and L. Weiland, "Prediction of the ionic polymer transducer sensing of shear loading," *Smart Mater. Struct.*, vol. 20, no. 9, pp. 094013-1–094013-9, 2011.

[8] Y. Bahramzadeh and M. Shahinpoor, "Dynamic curvature sensing employing ionic-polymer-metal composite sensors," *Smart Mater. Struct.*, vol. 20, pp. 094011-1–094011-7, 2011.

[9] H. Lei, C. Lim, and X. Tan, "Modeling and inverse compensation of dynamics of base-excited ionic polymercmetal composite sensors," *J. Intell. Mater. Syst. Struct.*, vol. 24, no. 13, pp. 1557–1571, 2013.

[10] F. Cellini, C. Intartaglia, L. Soria, and M. Porfiri, "Effect of hydrodynamic interaction on energy harvesting in arrays of ionic polymer metal composites vibrating in a viscous fluid," *Smart Mater. Struct.*, vol. 23, no. 4, pp. 045015-1-045015-15, 2014.

[11] Y. Cha, M.Verotti, H. Walcott, S. D. Peterson, and M. Porfiri, "Energy harvesting from the tail beating of a carangiform swimmer using ionic polymer metal composites," *Bioinspiration Biomimetics*, vol. 8, no. 3, pp. 036003-1–036003-15, 2013.
[12] Y. Cha, L. Shen, and M. Porfiri, "Energy harvesting from underwater torsional vibrations of a patterned ionic polymer metal composite," *Smart Mater. Struct.*, vol. 22, no. 5, pp. 055027-1–055027-13, 2013.
[13] S. D. Peterson and M. Porfiri, "Energy exchange between a vortex ring and an ionic polymer metal composite," *Appl. Phys. Lett.*, vol. 100, no. 11, pp. 114102-1-114102-4, 2012.
[14] K. J. Kim and M. Shahinpoor, "Ionic polymer-metal composites: II. Manufacturing techniques," *Smart Mater. Struct.*, vol. 15, pp. 65–79, 2003.
[15] L. N. Hao, Y. Chen, and Y. S. Zhao, "Research on enhanced performance of ionic polymer metal composite by multiwalled carbon nanotubes," *Mater. Res. Innovation*, vol. 19, no. 1, pp. 477–481, 2015.
[16] H. Lei, W. Li, and X. Tan, "Microfabrication of IPMC cilia for bio-inspired flow sensing," in *Electroactive Polymer Actuators and Devices (EAPAD) XIV*. Bellingham, WA, USA: SPIE Press, 2012.
[17] H. Lei, W. Li, G. Zhu, and X. Tan, "Evaluation of encapsulated ipmc sensor based on thick parylene coating," in *Proc. Conf. Smart Materials, Adaptive Struct. Intell. Syst.*, 2012, pp. SMASIS2012–7975.
[18] S. Sareh, J. Rossiter, A. Conn, K. Drescher, and R. E. Goldstein, "Swimming like algae: Biomimetic soft artificial cilia," *J. Royal Soc. Interface*, vol. 100, no. 78, pp. 20120666-1–20120666-12, 2013.
[19] B. Sivasubramanian and D. Kim, "Development, analysis, and comparison of electromechanical properties of buckypaper IPMC actuator," in *Electroactive Polymer Actuators and Devices (EAPAD) XIV*. Bellingham, WA, USA: SPIE, 2014.
[20] V. Palmre, D. Pugal, K. J. Kim, K. K. Leang, K. Asaka, and A. Aabloo, "Nanothorn electrodes for ionic polymer-metal composite artificial muscles," *Sci. Rep.*, vol. 4, pp. 6176-1–6176-10, 2014.
[21] Y. Cha, M. Aureli, and M. Porfiri, "A physics-based model of the electrical impedance of ionic polymer metal composites," *J. Appl. Phys.*, vol. 111, no. 2, pp. 124901-1–124901-14, 2012.
[22] C. Lim, H. Lei, and X. Tan, "A dynamic, physics-based model for base-excited IPMC sensors," in *Electroactive Polymer Actuators and Devices (EAPAD) XIV*. Bellingham, WA, USA: SPIE, 2012.
[23] Z. Sun, L. Hao, W. Chen, Z. Li, and L. Liu, "A novel discrete adaptive sliding-mode-like control method for ionic polymer-metal composite manipulators," *Smart Mater. Struct.*, vol. 22, no. 9, pp. 095027-1–095027-13, 2013.
[24] Y. Xiong, Y. Chen, Z. Sun, L. Hao, and J. Dong, "Active disturbance rejection control for output force creep characteristics of ionic polymer metal composites," *Smart Mater. Struct.*, vol. 23, no. 7, pp. 075014-1–075014-10, 2014.
[25] M. Aureli and M. Porfiri, "Nonlinear sensing of ionic polymer metal composites," *Continuum Mech. Thermodynamics*, vol. 25, no. 2, pp. 273–310, 2013.
[26] L. Hao and Z. Li, "Modeling and adaptive inverse control of hysteresis and creep in ionic polymer-metal composite actuators," *Smart Mater. Struct.*, vol. 19, no. 2, pp. 025014-1–025014-6, 2010.
[27] K. Farinholt and D. J. Leo, "Modeling of electromechanical charge sensing in ionic polymer transducers," *Mech. Mater.*, vol. 36, pp. 421–433, 2004.
[28] K. Oguro, N. Fujiwara, K. Asaka, K. Onishi, and S. Sewa, "Polymer electrolyte actuator with gold electrodes," in *Electroactive Polymer Actuators and Devices (EAPAD) XIV*. Bellingham, WA, USA: SPIE, 1999.
[29] S. J. Kim, D. Pugal, J. Wong, K. J. Kim, and W. Yim, "A bio-inspired multi degree of freedom actuator based on a novel cylindrical ionic polymer-metal composite material," *Robot. Auton. Syst.*, vol. 62, no. 1, pp. 53–60, 2014.
[30] T. Stalbaum, D. Pugal, S. E. Nelson, V. Palmre, and K. J. Kim, "Physics-based modeling of mechano-electric transduction of tube-shaped ionic polymer-metal composite," *J. Appl. Phys.*, vol. 117, no. 11, pp. 114903-1–114903-8, 2015.
[31] L. Shen, Y. Cha, A. Shams, and M. Porfiri, "Fabrication and buckling analysis of ionic polymer metal composite pipes," *Smart Mater. Struct.*, vol. 22, no. 10, pp. 105032-1–105032-11, 2013.
[32] H. Lei and X. Tan, "Fabrication and characterization of a two-dimensional IPMC sensor," in *Electroactive Polymer Actuators and Devices (EAPAD)*. San Diego, CA, USA: SPIE, 2013.
[33] S. Nemat-Nasser and J. Li, "Electromechanical response of ionic polymer-metal composites," *J. Appl. Phys.*, vol. 87, no. 7, pp. 3321–3331, 2000.
[34] H. Lei and X. Tan, "A novel tubular thin-wall IPMC sensor capable of two-dimensional sensing: Fabrication, characterization and modeling," in *Proc. ASME Conf. Smart Mater., Adaptive Struct. Intell. Syst.*, 2014, pp. SMASIS2014–7594.
[35] T. Ganley, D. L. S. Hung, G. Zhu, and X. Tan, "Modeling and inverse compensation of temperature-dependent ionic polymer-metal composite sensor dynamics," *IEEE Trans. Mechatron.*, vol. 16, no. 1, pp. 80–89, Feb. 2011.
[36] Z. Chen, X. Tan, A. Will, and C. Ziel, "A dynamic model for ionic polymer-metal composite sensors," *Smart Mater. Struct.*, vol. 16, pp. 1477–1488, 2007.
[37] C. R. Calladine, *Theory of Shell Structures*. Cambridge, U.K.: Cambridge Univ. Press, 1989.
[38] G. A. Baker and P. Graves-Morris, *Padé Approximants*. New York, NY, USA: Cambridge Univ. Press, 1996.
[39] J. M. Gere, *Mechanics of Materials*. Belmont, CA, USA: Thomson Learning, 2004.
[40] H. Lei, C. Lim, and X. Tan, "Humidity-dependence of IPMC sensing dynamics: Characterization and modeling from a physical perspective," *Meccanica*, pp. 1–11, 2015. doi: 10.1007/s11012-015-0164-6.
[41] H. Lei, W. Li, and X. Tan, "Encapsulation of ionic polymer-metal composite (ipmc) sensors with thick parylene: Fabrication process and characterization results," *Sensors Actuators: A, Phys.*, vol. 217, pp. 1–12, 2014.

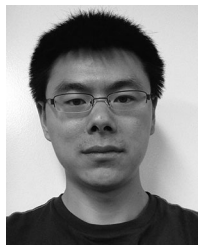

Hong Lei received the B.Eng. and M.Eng. degrees from the Beijing University of Aeronautics and Astronautics, Beijing, China, in 2006 and 2009, respectively, and the Ph.D. degree in electrical and computer engineering from Michigan State University, East Lansing, MI, USA, in 2015.

He joined Smart Microsystems Laboratory, Michigan State University, in August 2009, and is currently a Research Associate at this lab. His research is focused on the modeling of sensing properties and the development of sensor application for ionic polymer-metal composite materials.

Montassar Aidi Sharif received the Bachelor's and Master's degrees in mechatronics engineering from the Al-Khwarizmi College of Engineering, University of Baghdad, Baghdad, Iraq, in 2006 and 2009, respectively. He started working toward the Ph.D. degree at the Smart Microsystems Lab, Department of Electrical and Computer Engineering, Michigan State University, East Lansing, MI, USA, in August 2013.

His current research is focused on ionic polymer-metal composite flow sensors.

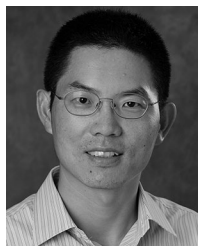

Xiaobo Tan (S'97–M'02–SM'11) received the B.Eng. and M.Eng. degrees in automatic control from Tsinghua University, Beijing, China, in 1995 and 1998, respectively, and the Ph.D. degree in electrical and computer engineering from the University of Maryland, College Park, MD, USA, in 2002.

From September 2002 to July 2004, he was a Research Associate at the Institute for Systems Research, University of Maryland. He joined the faculty of the Department of Electrical and Computer Engineering, Michigan State University, East Lansing, MI, USA, in 2004, where he is currently a Professor. His research interests include modeling and control of systems with hysteresis, electroactive polymer sensors and actuators, and bio-inspired underwater robots and their application to environmental sensing.

Dr. Tan has served as an Associate Editor/Technical Editor for *Automatica*, IEEE TRANSACTIONS ON MECHATRONICS, and *International Journal of Advanced Robotic Systems*. He served as the Program Chair of the 2011 International Conference on Advanced Robotics, and the Finance Chair of the 2015 American Control Conference. He has coauthored one book and more than 60 peer-reviewed journal papers, and holds one US patent. He is a recipient of NSF CAREER Award (2006), MSU Teacher-Scholar Award (2010), and several Best Paper Awards.